Simulation of guided-wave ultrasound propagation in composite laminates: Benchmark comparisons of numerical codes and experiment

Cara A. C. Leckey[a,*], Kevin R. Wheeler[b], Vasyl N. Hafiychuk[c], Halyna Hafiychuk[c], Doğan A. Timuçin[b]

[a]*NASA Langley Research Center, Hampton, VA 23681*
[b]*NASA Ames Research Center, Moffett Field, CA 94035*
[c]*Stinger Ghaffarian Technologies, Inc., Moffett Field, CA 94035*

Abstract

Ultrasonic wave methods constitute the leading physical mechanism for nondestructive evaluation (NDE) and structural health monitoring (SHM) of solid composite materials, such as carbon fiber reinforced polymer (CFRP) laminates. Computational models of ultrasonic wave excitation, propagation, and scattering in CFRP composites can be extremely valuable in designing practicable NDE and SHM hardware, software, and methodologies that accomplish the desired accuracy, reliability, efficiency, and coverage. The development and application of ultrasonic simulation approaches for composite materials is an active area of research in the field of NDE. This paper presents comparisons of guided wave simulations for CFRP composites implemented using four different simulation codes: the commercial finite element modeling (FEM) packages ABAQUS, ANSYS, and COMSOL, and a custom code executing the Elastodynamic Finite Integration Technique (EFIT). Benchmark comparisons are made between the simulation tools and both experimental laser Doppler vibrometry data and theoretical dispersion curves. A summary is given of the accuracy of simulation results and the respective computational performance of the four different simulation tools.

Keywords: Ultrasound, guided wave, simulation, composite, delamination

1. Introduction

In recent decades, the aerospace industry has seen a rapid growth in the use of composite materials since this class of materials can enable advanced lightweight aircraft and spacecraft designs. While the increased use of composites is expected to continue due to their weight benefit and tailorability, these materials also pose unique challenges for post-manufacture certification; as well as for in-service inspection. Common defect types that occur in composite materials include delamination damage, porosity, and microcracking [1, 2]. Practical and reliable nondestructive evaluation (NDE) and structural health monitoring (SHM) methods for detection and quantification of such defects/damage are of key importance for enabling the certification and ensuring the safety of aerospace vehicles with composite parts.

Currently, ultrasonic methods constitute the leading physical mechanism used for NDE and SHM of aerospace composite materials such as carbon-fiber-reinforced polymer (CFRP) laminates. Computational ultrasound models (analytical, semi-analytical, and numerical) solve the equations of motion for a composite part with specified initial and boundary conditions. Numerical methods such as finite element (FE) or finite difference (FD) can incorporate detailed composite material properties and complex damage morphologies into ultrasound models. These high-fidelity ultrasonic wave propagation models can enable optimal NDE and SHM hardware, data processing tool designs, and inspection methodologies to provide the desired inspection accuracy, reliability, efficiency, and coverage for composite structures.

Within the last decade, a growing number of authors have reported the implementation of three-dimensional (3D) ultrasonic numerical simulations for composite materials. Ng *et al.* discussed the need for including three-dimensional (3D) damage representations in wave simulations of composite laminates, and used a 3D FE method to simulate guided waves in a quasi-isotropic laminate [3]. These authors modeled each individual layer in the quasi-isotropic laminate, using the assumption of a homogeneous orthotropic material properties for each ply. Simple circular-geometry delaminations of various radii were incorporated into the simulations and the FE results were then compared to analytical models. Singh *et al.* reported using a commercial FE code to simulate guided waves in a composite laminate with homogenized material properties through the thickness (*i.e.*, individual ply layers were not simulated) [4]. This team studied guided-wave interaction with a simulated cone-shaped defect representing impact damage. Leckey *et*

al. used a custom 3D finite integration code to study guided-wave propagation in anisotropic composite laminates (simulating each ply layer), and incorporated a realistic damage geometry using x-ray computed tomography data of impact-induced delamination damage [5]. More recently, Murat *et al.* report using a custom FE code to simulate guided-wave propagation in a cross-ply composite laminate, and specifically studied wave interaction with a square-shaped delamination [6].

The intent of the simulation studies reported in this paper is to determine benchmark comparisons establishing the accuracy and the computational requirements of various numerical codes for simulating ultrasonic guided-wave propagation in composite laminates. Several considerations enter into the practical implementation of a simulation code, thereby rendering each code unique in its details. These include:

- represented spatial scale (fiber-, ply-, or plate-level specification of constitutive relationships, fine or coarse representation of defects);

- spatio-temporal discretization of governing equations of motion and boundary conditions (mesh shape, mesh density);

- spatio-temporal duration of simulation (localized *vs.* extended response, space-time *vs.* wavenumber-frequency domain computation);

- solver parameters (controlling stability, convergence, *etc.*).

The choices made in fixing these details for a particular problem must depend, to a large degree, on the experimental scenario that the numerical simulation is intended to represent. The chosen parameters essentially represent a trade-off between the accuracy and the stability of the code on the one hand, and its memory and computational runtime requirements on the other. While custom-developed codes can provide the user with significant flexibility in some of these details, taking proper advantage of such a capability requires a deep understanding of both the underlying physics and its numerical implementation on the part of the user. On the other hand, commercial software codes frequently "hard-wire" some of these details in order to provide easy access to a larger community of users. Proper validation of simulation tools is required for both custom and commercial codes in order to ensure that the simulation setup and implementation are appropriate for the physics experiment under study.

In making an informed decision about the choice and the use of a computational modeling tool, the availability of benchmark problems with associated experimental data sets and simulation studies is indispensable. In this paper, we report on two simulation case studies involving guided ultrasonic waves in (i) a pristine CFRP laminate, and (ii) a CFRP laminate containing a single delamination-type defect of known size and location. Guided wave simulations were performed for these simulation cases using four different simulation codes: the commercial finite element modeling (FEM) packages ABAQUS, ANSYS, and COMSOL, and a custom code executing the Elastodynamic Finite Integration Technique (EFIT). COMSOL, ANSYS and ABAQUS are implemented with an implicit time solution. Additionally, ABAQUS is also implemented in an explicit time-stepping mode, and EFIT is also explicit in time. For both CFRP simulation cases, comparisons are performed between the simulated guided wavefield results from the four different simulation tools and wavefield results from experiment. In addition, all wavefield results are compared with dispersion curve predictions.

In Section 2, the geometry and composition of the pristine and delaminated experimental specimens are documented, along with the experimental setup including the excitation source. Section 3 then gives a detailed description of the simulation tools used in this benchmarking study, focusing particularly on their resolution and stability requirements. Section 4 describes the experimental and simulation results for the pristine specimen, comparing codes on the basis of their wavenumber spectra and group velocity values. Section 5 reports on the experimental and simulation results for the delaminated specimen, showing time-domain wavefield images as well as wavenumber spectra for the various codes. Section 6 discusses the computational resource requirements of each simulation tool. Lastly, Section 7 summarizes the findings of this benchmarking study and discusses areas of future work.

2. Experimental Setup

2.1. Composite specimens

In order to generate an example problem and representative data sets that anchor the simulation studies, two IM7/8552 CFRP test panels were fabricated at NASA Langley Research Center. IM7/8552 is a high-performance composite material used for aerospace applications. Table 1 lists elastic material properties for a single ply of IM7/8552 from values reported in the

Table 1: Single-ply IM7/8552 material properties. Fiber orientation is taken to be along the $x_1 = x$ axis, while the out-of-plane direction is along the $x_3 = z$ axis (laminate thickness axis); ρ, E, G, and ν denote density, Young's modulus, shear modulus, and Poisson's ratio, respectively.

Property	Symbol	Value
density (kg/m^3)	ρ	1570.0
Young's moduli (GPa)	E_1	171.4
	E_2	9.08
	E_3	9.08
shear moduli (GPa)	G_{12}	5.29
	G_{13}	5.29
	G_{23}	2.80
Poisson's ratios (—)	ν_{12}	0.320
	ν_{13}	0.320
	ν_{23}	0.5

scientific literature [22, 23, 24]. The panels were made using eight plies of IM7/8552 material cured in a cross-ply layup of $[0_2/90_2]_s$ with an overall thickness of 0.92 mm. One of the panels was pristine while the other had a double-layered Teflon film in the shape of a 20 mm by 20 mm square inserted between the second and third ply layers (see Figure 1). The Teflon insert served to mimic a delamination-type defect.

2.2. Excitation and Measurement

For both specimens a GE Inspection Technologies Gamma Series (TCG-999) 0.5 MHz contact piezo-electric transducer (PZT) was used to excite guided ultrasonic waves in the composite specimens. The transducer is a disk-shaped actuator with an overall diameter of 19 mm. The transducer was coupled to one side of the panel, see Figure 1, and was driven by a 300 kHz 3-cycle Hann-windowed sine wave. The center frequency of the excitation signal was chosen to ensure that only two guided wave modes would be generated for the thicknesses of the experimental specimens. This choice of frequency therefore ensures that the benchmark comparisons are not

overly complicated by the simultaneous presence of numerous guided-wave modes.

A Polytec OFV-505 laser Doppler vibrometer (LDV) connected to an OFV-5000 controller with a 1 MHz high-frequency cutoff was used to collect experimental data for the benchmark comparisons. The LDV is attached to a two-axis scanning system to acquire out-of-plane velocity measurements on a pre-defined Cartesian grid. The LDV is set up to collect data for the panel surface opposite to the PZT actuator, see Figure 1. A 0.2 mm spatial grid spacing in both $\hat{x}$ and $\hat{y}$ directions was used for collecting data on both the pristine and the delaminated panels. The out-of-plane velocity signals recorded by the LDV were digitized at a sampling rate of 20 MHz.

3. Computational Setup

The four numerical simulation tools used in this study were a custom implementation [5] of the 3D Elastodynamic Finite Integration Technique (EFIT) [7] along with three widely used commercial FE codes: COMSOL [31], ABAQUS [29], and ANSYS [30]. These numerical tools were used to simulate the experimental scenarios of interest described in Section 2. The specific implementation details for each simulation tool are discussed below.
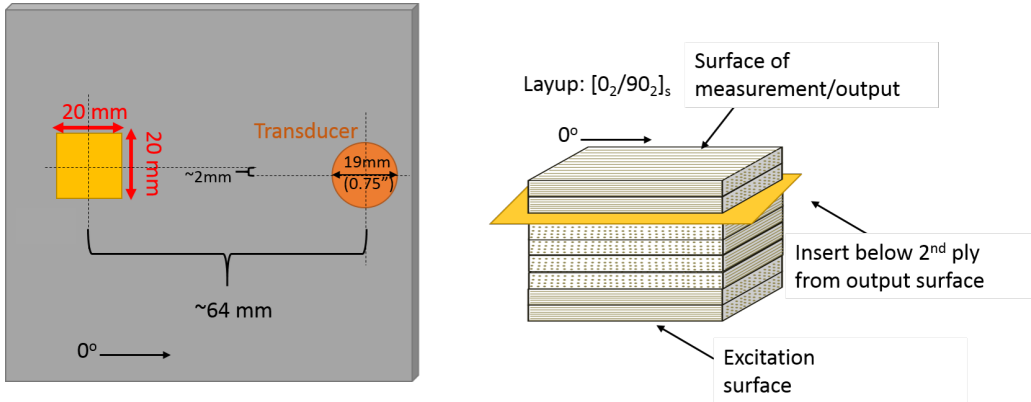

Figure 1: Details of the composite specimen containing the Teflon insert: Top view (left) showing the dimensions and relative positions of the actuator and the Teflon insert, and zoomed-in side view (right) showing the through-thickness panel layup, the depth location of the Teflon insert, and the excitation and measurement/output surfaces.

6

3.1. Common setup

The material property values listed in Table 1 were used to construct ply-level stiffness matrices, with the assumption that each ply is transversely isotropic [1] and with suitable rotations applied to account for the $[0_2/90_2]_s$ cross-ply layup. Each of the eight ply layers was taken to be 0.115 mm thick, thus matching the measured total thickness of the experimental specimens. The plies were rigidly tied to their neighbors except at the delaminated region, which was modeled as a 20-mm square stress-free (*i.e.*, non-bonded) contact surface between the second and third ply layers. COMSOL provides a Thin Elastic Layer option with two adjustable parameters (spring and damping constants), but this option was not exercised here in order to obtain results more directly comparable to the other simulation tools. Additionally, it is noted that prior work has shown good agreement between simulation and experiment by modeling delaminated regions with stress-free boundaries [28].

A 3-cycle Hann windowed sine wave (matching the experimental scenario) was applied as a time-dependent displacement boundary condition over the 19-mm diameter circular footprint of the actuator indicated in Figure 1. The top and bottom surfaces of the simulated domain were taken to be stress-free for all simulations. EFIT, ABAQUS Explicit, and ANSYS Implicit applied stress-free boundary conditions to all edges, while COMSOL and ABAQUS implicit applied absorbing boundary conditions to plate edges in order to reduce simulation run time. The FE simulations were performed for a 6 cm $\times$ 9 cm area, using a symmetry boundary at the location of the actuator to reduce the simulation size (see Figure 3). The EFIT simulation was performed for 6 cm $\times$ 120 cm area in order to include the entire actuator (as implementation of a symmetry boundary is not currently an option in the EFIT custom code). The simulations were run from $t = 0$ to $T_{\text{sim}} = 60$ μs. Finally, the top-surface out-of-plane velocity field $v \equiv \mathrm{d}z/\mathrm{d}t$ was output from each simulation by interpolating on a common space-time grid over the simulated region (x, y) and time interval $t \in [0, T_{\text{sim}}]$.

The dispersion curves for the guided wave modes in the pristine structure were computed using DISPERSE software [25], which uses the global matrix method and a root finder to determine the mode eigenvalues. Figure 2 shows the symmetric-mode (red) and antisymmetric-mode (blue) dispersion curves. The dispersion curves confirm that the only guided waves which propagate at the center frequency of the excitation, $f_{\text{exc}} = 300$ kHz, and plate thickness
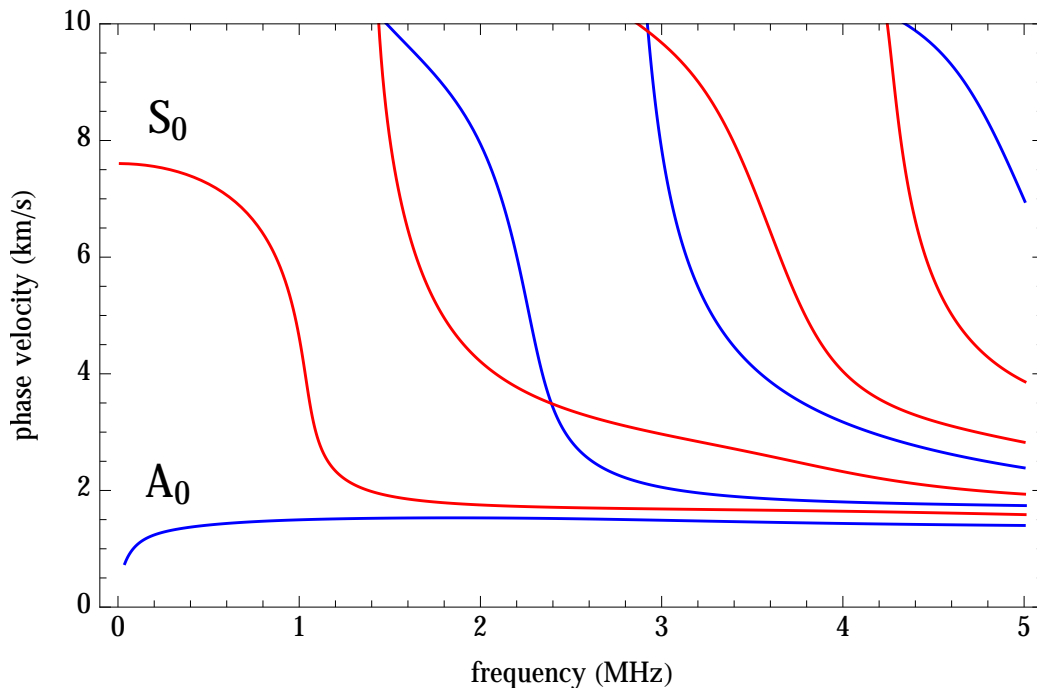
Figure 2: Guided wave dispersion curves showing phase velocity versus frequency-thickness for the crossply layup along the 0 degree direction.

are indeed an antisymmetric A_0 slow mode and a symmetric S_0 fast mode, with all higher-order modes cut off at this frequency.

3.2. Elastodynamic Finite Integration Technique

3.2.1. Overview

EFIT is an explicit numerical method that is similar to the standard staggered-grid FD approach [7]. A benefit of the EFIT method is that it leads to straightforward equations that can be readily implemented using any programming language. As a result, the user has direct control over every mathematical and computational operation performed by the code. Furthermore, the equations are practical to parallelize for use on computing clusters and multicore machines. The code implemented for the studies in this work is written in C++, and is explicitly parallelized using Message Passing Interface (MPI). The simple form of the mathematical equations also enables the development of an extremely memory-efficient code [8]. These computational benefits may allow for the implementation of larger 3D simulations

8

than are feasible with current commercial packages. However, a downside to the use of a custom code is that it may not be as flexible or user-friendly as commercial simulation packages.

During the last few decades, since the finite integration technique was applied to elastodynamics by Fellinger and Langenberg [9], many authors have reported using EFIT to explore ultrasonic NDE applications. However, most prior work in the literature has been restricted to 2D or has focused on isotropic materials [10, 11, 12, 13, 14, 15]. Within the last decade, the increased availability of multicore and cluster computing resources has led to full 3D EFIT implementations, albeit still mostly focused on isotropic materials [16, 17, 18, 19, 20, 21]. Recently, Leckey *et al.* developed a 3D EFIT code for application to aerospace composite materials [5]. An overview of the finite integration technique can be found in a prior review paper by Marklein [13].

3.2.2. Grid sizing and stability requirements

The EFIT approach implemented for the studies reported in this paper uses a simple-cubic Cartesian grid where the three velocity components (one out-of-plane and two in-plane terms) and six stress components (three normal and three shear stress terms) are calculated for each grid cell. For both simulation scenarios (pristine and delamination case), each ply layer of the laminate layup was modeled. Stress-free boundary conditions were implemented at all simulation edges.

Unlike FE approaches where quadratic or other basis functions can be used, in the EFIT code the velocity and stress values are treated as constant within a single grid cell. The EFIT method has specific requirements for the spatial and temporal step sizes to ensure accuracy and stability. As reported in the literature [19], a minimum of 8 spatial grid points are required per smallest wavelength in the simulation in order to capture the dynamics of the ultrasonic wave behavior. Additionally, the well-known Courant–Friedrichs–Lewy (CFL) stability criterion imposes the strict requirement

$$\Delta t \leq \frac{\Delta x}{\sqrt{3}\, c_{\max}} \qquad (1)$$

between the spatial and temporal step sizes Δx and Δt, where $c_{\max}$ is the maximum speed of ultrasonic wave propagation in the simulation [10].

The EFIT simulations for both the pristine and defect specimen used a spatial step equal to 4 steps per ply layer (28.75 μm) and a time step size of

9

2.19 ns. This spatial step size was chosen to based on grid refinement studies discussed in Section 3.6 that showed a consistent corresponding group velocity result when 4 or more grid points per ply layer were used. For the 8 ply thick composite laminate with total thickness 0.92 mm and the 300 kHz excitation frequency, the resulting frequency-thickness product combined with the curves in Figure 2 leads to an S_0 mode phase velocity of $\simeq$ 7,510 m/s to be used for $c_{\max}$ in (1). It is seen that the above choices for space-time discretization satisfy the CFL condition.

3.3. COMSOL

3.3.1. Overview

COMSOL Multiphysics [31] is a versatile FE analysis software that is designed to investigate coupled multi-physics problems. In the present study, only the Solid Mechanics module version 5.2 was employed in modeling ultrasonic guided-wave propagation in the anisotropic composite structure depicted in Figure 1.

In contrast with EFIT's explicit time stepping approach described above, COMSOL uses an implicit scheme involving the parallel sparse direct solver MUMPS. The iterative time solver was the generalized-α method with intermediate solver steps, a linear predictor, and a maximum time step of 50 ns. The absolute tolerance of the time-dependent solver used a global method of scaling with a specified tolerance of 0.001. However, as discussed further in Section 6, it was found that specifying a manual time step size reduced the computation time by an order of magnitude compared to allowing COMSOL to determine the time step at each iteration.

3.3.2. Mesh Sizing and Stability Requirements

COMSOL simulations employed free triangular meshes swept in the $x_3 = z$ direction. Specifically, a free triangular planar boundary mesh was established on the top surface with a minimum mesh size that varied from 0.8 mm in the pristine regions to 0.4 mm in the delaminated region as well as near the PZT actuator. This boundary mesh was then swept through the panel thickness with a specification of two grid points per ply layer 57.5 μm. The meshing method was chosen in order for the top observation surface to consist of only one flat domain, which simplified the comparison of simulation output with experimental data.

Three practical measures were taken to improve the simulations. The computational domain was terminated at the mid-section of the PZT actu-

ator, with a symmetry boundary condition imposed along this edge, which cut down on computational time. Additionally, a two-parameter exponentially increasing Rayleigh viscous damping was implemented in the 1-cm thick region along the boundary of the computational domain. This helped to prevent the simulated wavefield from becoming cluttered with simulation edge reflections. Furthermore, as discussed in Section 6, a manual time step size was chosen to reduce computation time.

3.4. ABAQUS

3.4.1. Overview

ABAQUS [29] is a general-purpose finite-element modeling code that is highly popular in the composites community. A composite laminate may be modeled in (at least) three different ways in ABAQUS version 2016, which was used for this study. The shell model is strictly 2D, and therefore not suitable for investigating the through-thickness mode profiles, which was of interest here. The continuum model allows one to generate a ply-by-ply 3D construction of the laminate explicitly. ABAQUS also offers a Solid Composite Layup module that is dedicated for convenient modeling of CFRP type laminates. Both of these latter approaches allow a full 3D wavefield simulation, and were employed in this study.

ABAQUS provides two options for dynamic analysis: implicit (I) and explicit (E). ABAQUS/I is the standard approach, and employs an implicit time integration scheme based on the Hilber–Hughes–Taylor algorithm, which is known for its well-conditioned Jacobian matrix. However, the need to invert a large Jacobian matrix at each time step can become computationally expensive. On the other hand, ABAQUS/E employs the central-difference operator for time integration, which does not require matrix inversion and therefore can be much more efficient. However, ABAQUS/E simulations are subject to the same strict CFL condition (1) as EFIT, whereas ABAQUS/I time integration is stable for a wider range of parameters and can be traded off against solution accuracy if desired. ABAQUS/E is also limited to fewer spatial mesh element types. Both analysis methods were pursued in this study in order to exhibit the desirable features of each approach.

3.4.2. Mesh Sizing and Stability Requirements

Among various options available in ABAQUS, we used C3D8R hexahedral elements, which are 8-node linear bricks with reduced integration. In the (x, y) plane for ABAQUS/I, the pristine and delaminated regions were

11

meshed at 0.5 mm and 0.2 mm resolution, respectively, while there were 16 grid points (2 per ply layer) along the z direction. For ABAQUS/E the (x, y) plane used a mesh size of 0.2 mm in the pristine region and 0.1 mm in the defect region.

Both implicit and explicit schemes have automatic time stepping, but this feature must be used with some care. For the ABAQUS/E simulations, the initial time step was set to 1 ns, and was found to never exceed 5 ns. For ABAQUS/I simulations, on the other hand, the time step was observed to increase substantially in the automatic setting, and therefore had to be "manually" forced to remain below 0.1 μs. This manual intervention was necessary because under the automatic setting the time-stepping algorithms do not have a direct connection to the underlying physics being performed. Therefore, human expertise is required to appropriately set the time-stepping.

Finally, for ABAQUS/I simulations, the computational domain was surrounded with an inhomogeneous Rayleigh viscous damping zone to absorb the outgoing waves, as described above for COMSOL. Attempting to implement the same scheme for ABAQUS/E led to an extremely small ($\sim$ ps) time stepping requirement, which far exceeded the memory and run-time resources available and was therefore not feasible. Therefore stress-free boundaries were implemented at simulation edges for ABAQUS/E.

3.5. ANSYS

3.5.1. Overview

ANSYS [30] offers an extensive suite of FE simulation codes that covers a wide range of engineering physics. In this study, ANSYS Mechanical version 14.5 was used with a standard implicit solver. The ANSYS Workbench platform enables one to perform geometric modeling, material property definitions, meshing, pre-processing, post-processing, and visualization. The laminates modeled in this study were built ply by ply following the specifications given in Section 2.

3.5.2. Mesh Sizing and Stability Requirements

The triangular swept mesh used here matches the COMSOL mesh, while the mesh resolution of 0.5 mm (pristine) and 0.2 mm (defect) matches that of the ABAQUS mesh. Finer and coarser meshes were also simulated to establish the adequacy of resolution (see Section 3.6 below). ANSYS uses the APDL solver with the Newton–Raphson time integration method to solve
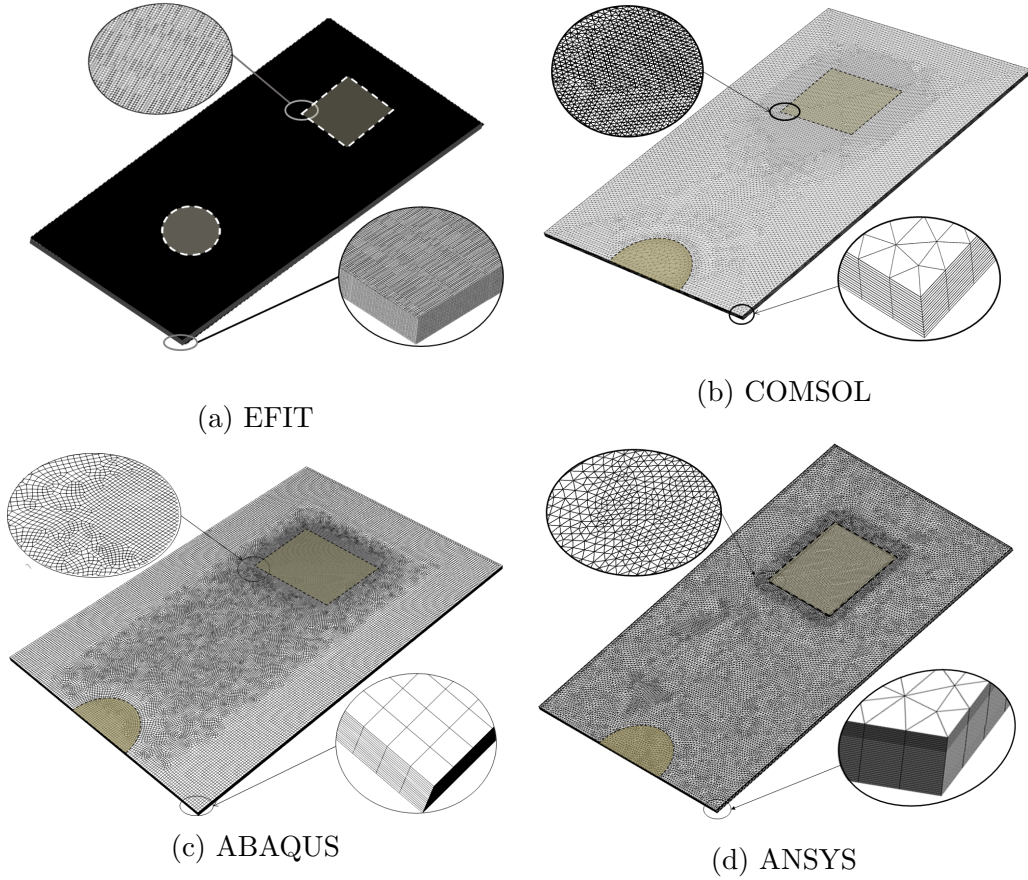
(a) EFIT

(b) COMSOL

(c) ABAQUS

(d) ANSYS

Figure 3: 3D mesh geometries for the simulation codes under study.

the system of equations on the mesh. In the simulations reported here, a fixed time step of 0.1μs was used, also matching ABAQUS/I.

3.6. Mesh convergence study

A snapshot of each simulation mesh, along with detailed views of the grids near the defect and through the panel thickness, is presented in Figure 3. Note in particular that the EFIT mesh is an order of magnitude denser in the (x, y) plane than the other code meshes.

In order to assess the adequacy of the benchmark mesh densities prescribed above and displayed in Figure 3, a mesh convergence study was conducted to investigate the change in the dominant A_0 mode group velocity as

the mesh resolution was varied. The mesh study was performed on a small plate problem for the same material properties, layup, and thickness (0.92 mm) of the pristine specimen described earlier. Figure 4 shows the trends for the various simulation codes, as well as the theoretical value from dispersion curves. It is interesting that for coarser meshes, COMSOL over-estimates the group velocity whereas the other FE codes and EFIT under-estimate this quantity for larger grid sizes. The simulation codes show improvement in estimating the group velocity as the mesh is made finer, which of course comes at the expense of increased computational time. At the mesh resolutions discussed earlier in this section, all codes are within 2 % of the theoretical value with respect to the group velocity metric, as discussed further in the following section.
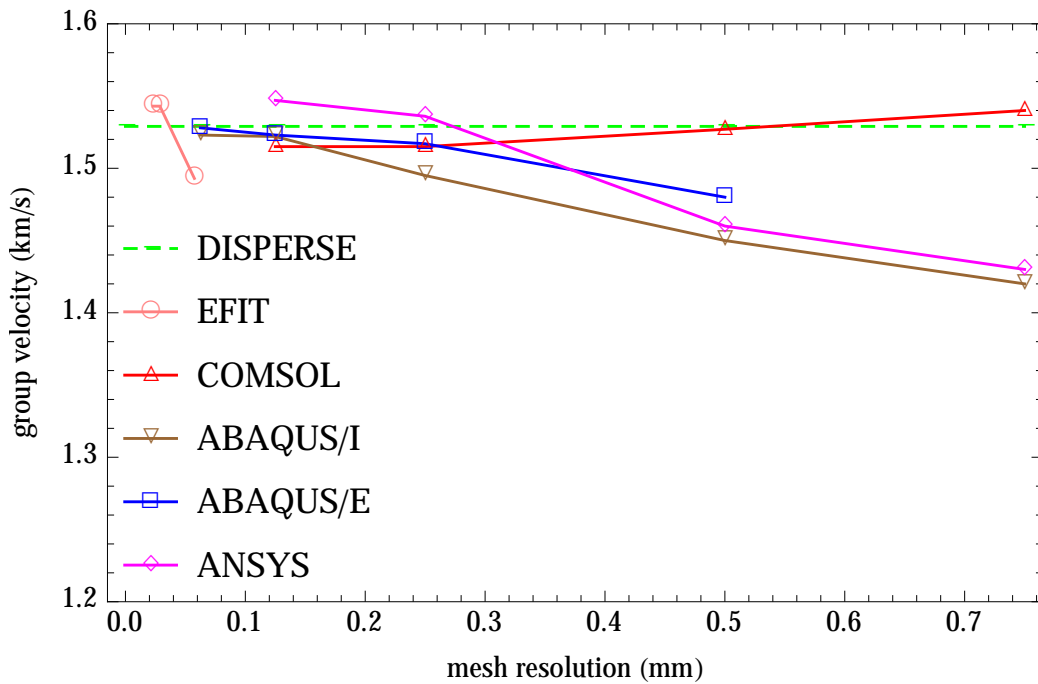

Figure 4: Dependence of the A_0 mode group velocity on the simulation mesh resolution.

4. Pristine specimen

4.1. Wavenumber comparison

Wavenumber domain analysis provides a quantitative approach for comparing experimental and computational wavefields, and is also helpful in identifying various guided-wave modes present in a data set. In this approach, a 3D fast Fourier transform (FFT) is performed on the given wavefield (in the present case, the top-surface out-of-plane velocity field $v(x, y, t)$) to obtain a spectral function $F(k_x, k_y, f)$ of wavenumbers (spatial frequencies) k_x, k_y and temporal frequency f. From this spectrum, a 2D slice can be extracted at the center frequency of excitation in order to assess the wavenumber content of the wavefield at that frequency.

Figure 5 shows $|F(k_x, k_y, f_{\text{exc}})|^2$ in the (k_x, k_y) plane for out-of-plane motion from the experimental data from the pristine specimen as well as for the corresponding simulation results (also out-of-plane motion). The dark disk at the center is due to the long-wave ("DC") motion of the entire panel. Based on the theoretical group velocity estimates at f_{exc} from DISPERSE (see Figure 2), it is deduced that the prominent dark outer ring corresponds to the higher out-of-plane amplitude A_0. A ring for the weaker out-of-plane amplitude S_0 is not readily visible in the plot. The other faint concentric rings are created by the shape of the excitation source. As discussed in [5], a point source excitation leads to the disappearance of these faint rings. As one would expect for a cross-ply CFRP laminate used in this study, the wavenumber of each guided mode is weakly direction-dependent.

Table 2 gives a quantitative comparison among experiment, theory (DISPERSE), and different simulation codes for the dominant (*i.e.*, A_0 mode) wavenumbers in directions parallel ($0°$) and perpendicular ($90°$) to the top-ply fiber direction. The table also reports the resolution of the measurement which corresponds to half of the pixel size of each plot in Figure 5 (which is determined by the bin size of the Fourier Transform operation). The wavenumber values show uniformly good agreement between theory and all simulation codes. The observed disagreement with experiment is attributed to deviations of the ply thicknesses, ply/fiber orientations, and material properties (primarily density) of the laboratory specimen from the idealized literature values used in simulations, see prior work by Leckey *et al.* for more details [5].
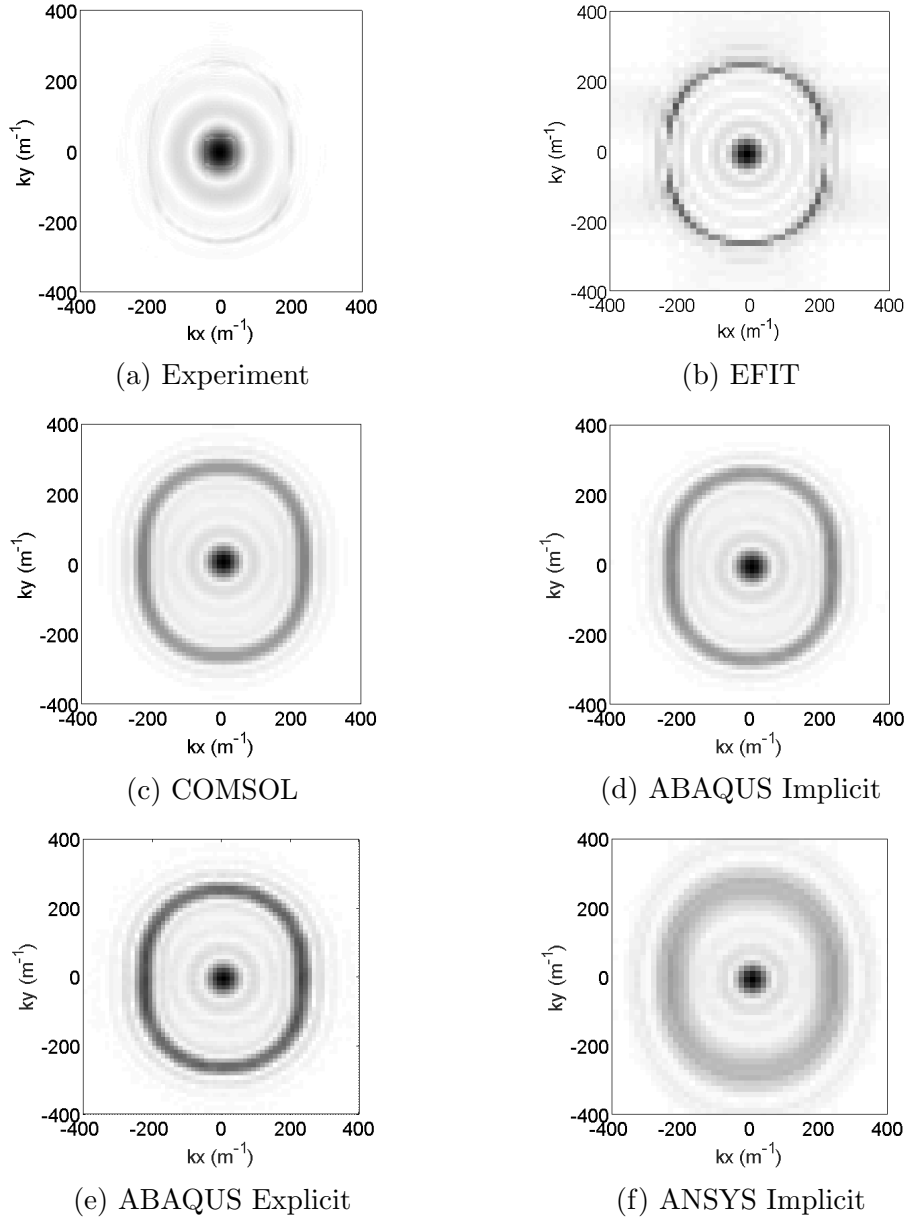
(a) Experiment

(b) EFIT

(c) COMSOL

(d) ABAQUS Implicit

(e) ABAQUS Explicit

(f) ANSYS Implicit

Figure 5: Wavenumber plots at the center excitation frequency, showing (k_x, k_y) for measured and simulated wavefields on the pristine specimen.

16

Table 2: Pristine specimen wavenumber comparison along the 0° direction (k_x) and 90° direction (k_y).

Method	k_x (1/m)		k_y (1/m)	
	Peak	*Resolution*	*Peak*	*Resolution*
Experiment	200.2	± 2.44	253.9	± 2.44
DISPERSE	229.5	—	269.5	—
EFIT/E	220.8	± 8.5	254.8	± 8.5
COMSOL/I	225.0	± 12.5	275.0	± 12.5
ABAQUS/I	225.0	± 12.5	262.5	± 12.5
ABAQUS/E	220.0	± 12.5	255.0	± 12.5
ANSYS/I	238.0	± 16.0	254.0	± 16.0

4.2. Group velocity comparison

Group velocity of the A_0 mode along the x axis (0° direction) was calculated from each of the time-domain (experimental and simulation) data sets. The group velocities were found by applying a Hilbert Transform to the time-domain data and tracking the peak amplitude position versus time. Due to the coarser spatial discretization of the FE codes, the Hilber transform was applied to the results of a moving-average filter of the time domain data. The spatial resolution of the time-domain data was maintained across different FE simulation mesh sizes by interpolating all the wavefields on a fixed grid. The fine spatial and time step sizes used for the EFIT simulation did not require averaging or interpolation. The theoretical A_0 mode group velocity value was determined from the dispersion curves generated by DISPERSE software (see Figure 2). Table 3 compares the group velocity results from experiment, theory, and the different simulation codes. Once again, all the simulation codes agree quite well with the theoretical prediction. As with the wavenumber comparisons, the dispersion curves and numerical codes show disagreement with experiment. As mentioned above, this agreement is expected to be due to differences in the idealized material properties used for the dispersion curves and numerical codes and the actual as-manufactured material properties [5].

Table 3: Pristine specimen group velocity (v_g) values along the 0° direction.

Method	v_g (km/s)
Experiment	1.698
DISPERSE	1.529
EFIT	1.543
COMSOL	1.515
ABAQUS/I	1.523
ABAQUS/E	1.531
ANSYS	1.547

5. Delaminated specimen

5.1. Time-domain comparison

In order to provide examples of the wavefield behavior for the delamination case, Figures 6 and 7 show experimental and simulated wavefield images in the (x, y) plane at two different points in time. In Figure 6, around $t = 30$ μs after the start of the excitation, the (fast) symmetric S_0 mode has interacted with the delamination, and in fact, multiple reflections as well as S_0-to-A_0 mode conversion above the delaminated region can be observed in the experimental result. In Figure 7, around $t = 40$ μs, the (slower) anti-symmetric A_0 mode is interacting with the delamination. It should be noted that all figures are shown with the same normalized amplitude color axis. Scattering patterns above the delamination region similar to those shown in the experimental result at 40 μs were observed for all simulation cases but at differing amplitude scales. For example, the selected color scaling for Figure 6 does not show the scattering above the defect region for EFIT or Abaqus/E results and also displays significantly lower amplitude scattering for the other simulation tools compared to experiment. These differences are expected, at least in part, to be the result of differences in the perfectly normal displacement created by the excitation sources used in the simulations versus the actual source incidence in the experimental case (which may actually create a small amount of shear displacement in addition to the normal displacement generated by the contact transducer).

The somewhat distorted experimental wavefronts seen in Figure 6(a) are attributable to non-symmetric imperfect coupling/mounting of the PZT ac-
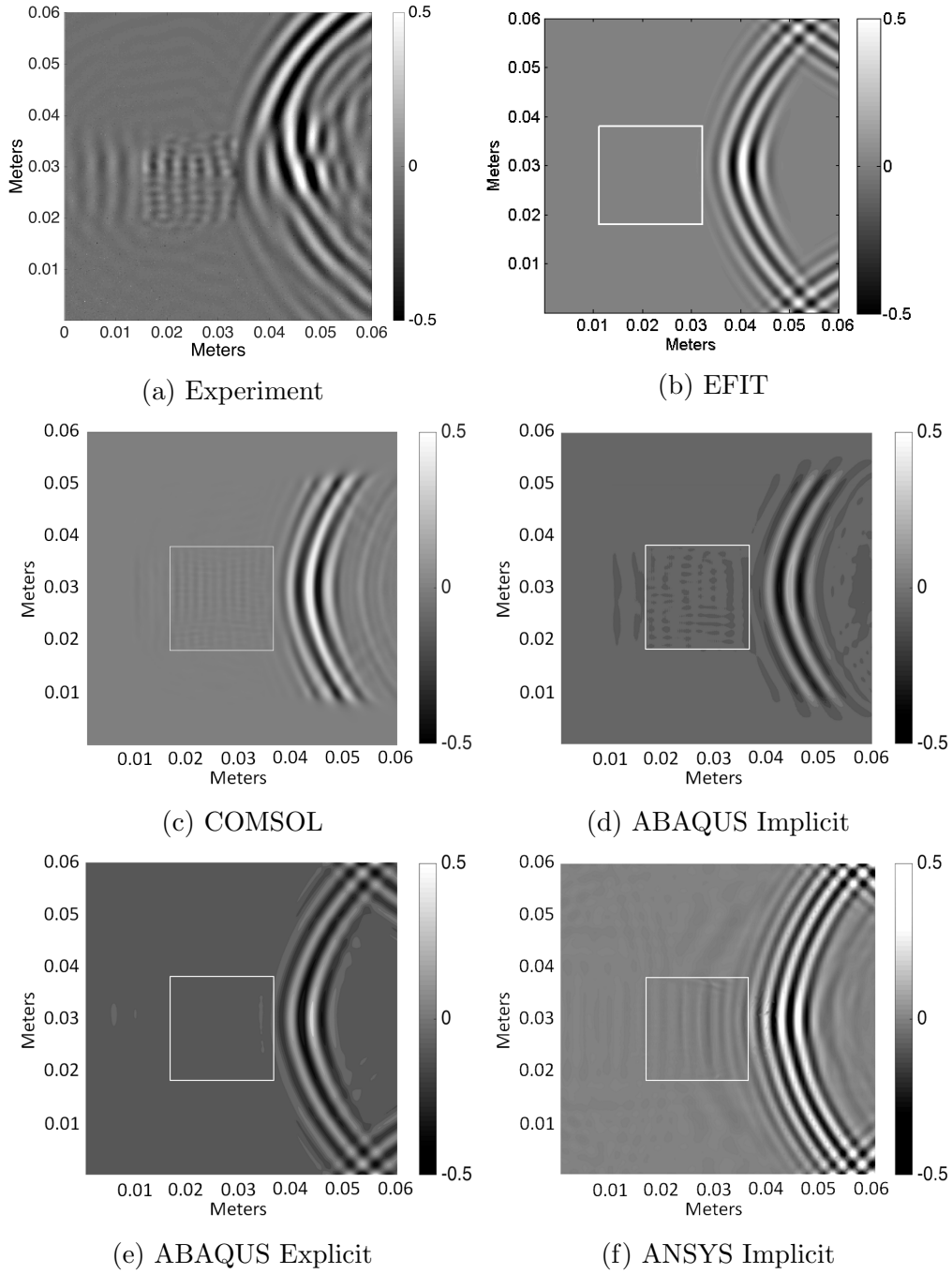
(a) Experiment

(b) EFIT

(c) COMSOL

(d) ABAQUS Implicit

(e) ABAQUS Explicit

(f) ANSYS Implicit

Figure 6: Wavefield images for the surface of the delaminated specimen at approximately 30 μs after the excitation.

(a) Experiment

(b) EFIT

(c) COMSOL
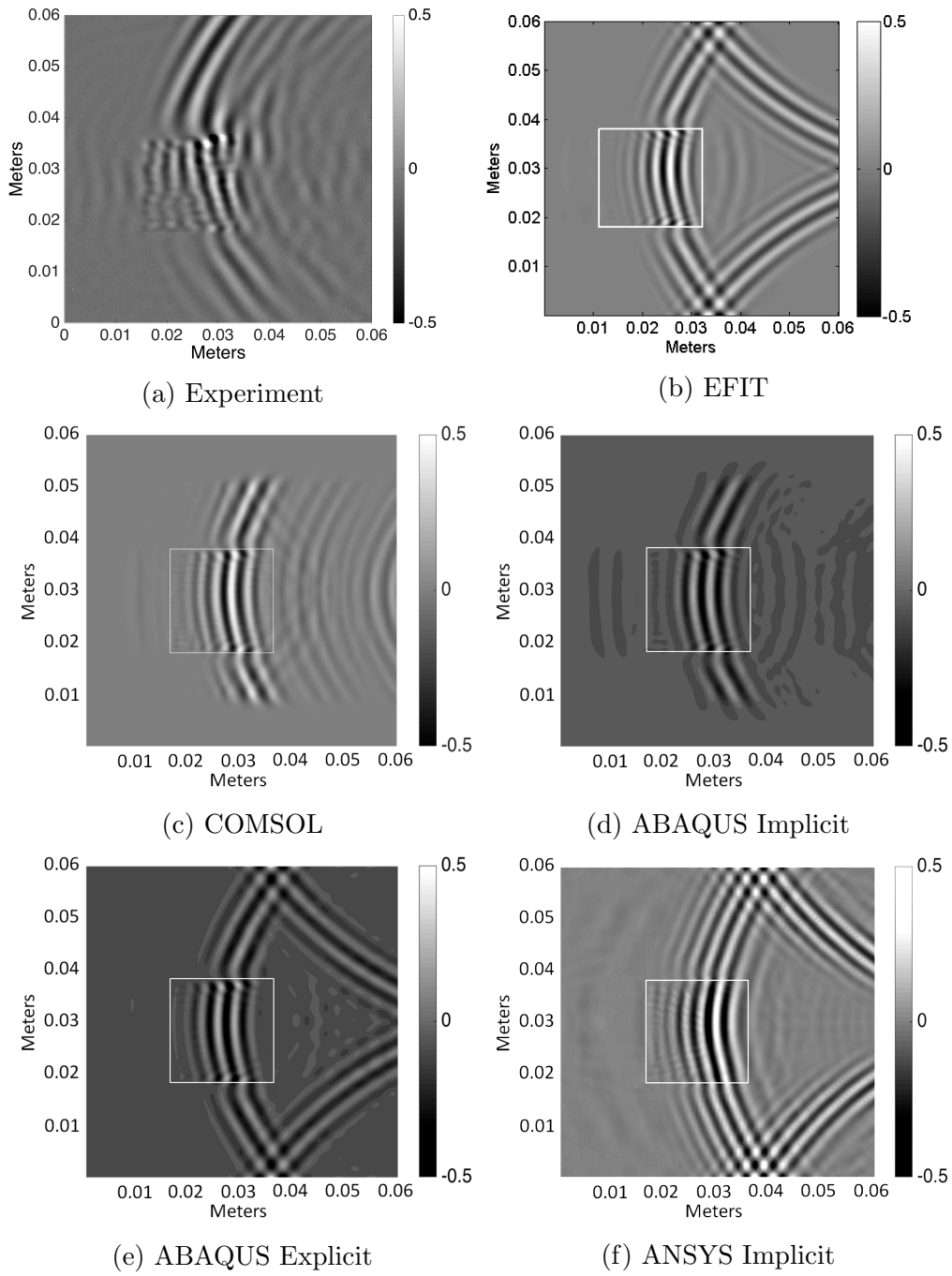
(d) ABAQUS Implicit

(e) ABAQUS Explicit

(f) ANSYS Implicit

Figure 7: Wavefield images for the surface of the delaminated specimen at approximately 40 μs after the excitation.

tuator on the panel. The nearly non-existent boundary reflections in parts
(c) and (d) indicate good (but not perfect) implementations the absorbing
boundary condition in COMSOL and ABAQUS/I around the edge of the
computational domain. The experimental wavefields are also devoid of any
edge reflections because the actual experimental panel is much larger than
the immediate neighborhood of the actuator and the defect to which the
simulated domains are limited as a practical matter.

5.2. Wavenumber comparison

Another feature that is observed in the time-domain wavefield images is
the change in the A_0 mode wavelength over the delaminated region. This
effect is readily observable in the wavenumber domain. Toward this end, the
Fourier Transform procedure explained in Section 4.1 is applied to each data
set for only the region of the wavefield over the delamination. The resulting
wavenumber plots are shown in Figure 8. The absolute value of the peak
wavenumber values in the 0° direction (k_x) are taken from the wavenum-
ber plots and compiled in Table 4. Note that in the wavenumber plots the
peak wavenumber falls in the negative $\hat{y}$ region due to the direction of wave
propagation. These values are to be contrasted with the peak k_x values
listed in Table 2 for the pristine specimen. The expected value based on
dispersion curves is also listed in Table 4. The change in wavenumber values
from the pristine case occurs due to the thinned region above the delamina-
tion since the defect essentially divides the laminate into two thinner plate
regions (above and below the defect). In fact, this connection between domi-
nant mode wavenumber and plate thickness can be established quantitatively
through the use of dispersion curves; allowing for estimation of defect depth
from experimental wavefield data [26, 27].

This observation sets up an important point that should be made here.
For simulations involving guided-wave phenomena, as in this paper, the use
of dispersion curves to determine the minimum wavelength and maximum ex-
pected wave velocities is indispensable in choosing the proper meshing for a
given problem. In simulation cases containing varying ply rotations through
the composite thickness, finer discretization may be required to accurately
capture the contributions of each ply layer. Furthermore, in regions where
the laminate is effectively separated into thinner layers by a delamination
type defect, additional grid points are generally needed in order to maintain
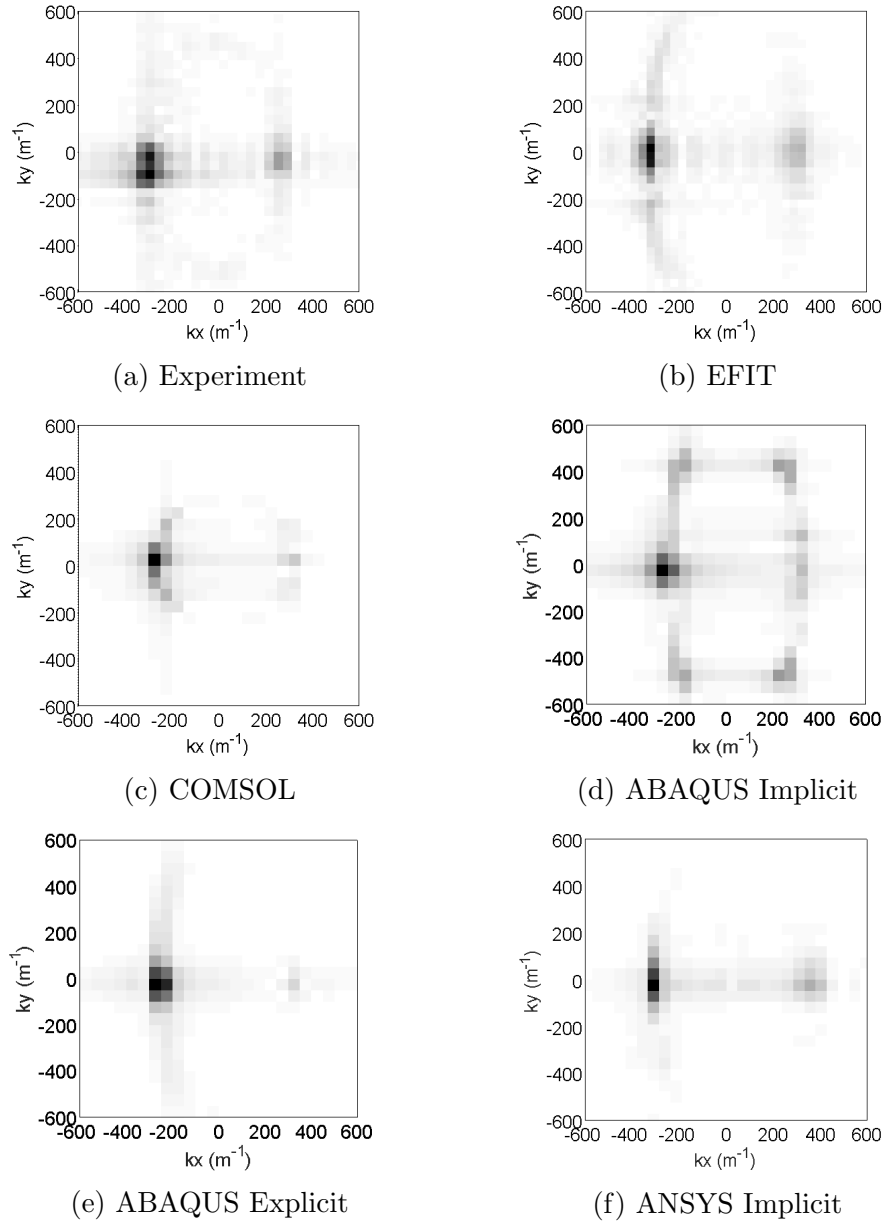simulation accuracy. As an example of the impact of spatial grid size on

(a) Experiment

(b) EFIT

(c) COMSOL

(d) ABAQUS Implicit

(e) ABAQUS Explicit

(f) ANSYS Implicit

Figure 8: Wavenumber plots in the (k_x, k_y) plane for measured and simulated wavefields over the defect region on the delaminated specimen.

Table 4: Delaminated specimen wavenumber comparison.

Method	k_x (1/m)	
	Peak	*Resolution*
Experiment	273.4	$\pm$ 19.5
DISPERSE	294.1	—
EFIT	305.7	$\pm$ 17.0
COMSOL	348.9	$\pm$ 25.0
ABAQUS/I	250.44	$\pm$ 12.5
ABAQUS/E	250.0	$\pm$ 12.5
ANSYS	290.0	$\pm$ 12.5

simulation accuracy, the EFIT wavenumber result reported in Table 4 represents a case with 8 spatial steps in the thin region above the defect. The wavenumber value above the defect is approximately 9 % different from the dispersion curve value and 11.1% different from experiment. When the same guided-wave simulation is run using only 4 spatial steps in the region above the defect, the wavenumber disagreement with the dispersion curve jumps to 23.6 % and to 30.8 % different from experiment.

6. Discussion of computational resources

Along with the physics-based observations made in the preceding sections, an important aspect of a simulation tool benchmarking exercise is to document the computational resources expended in obtaining the simulation results. A direct comparison between the various simulation codes is difficult since they are parallelized differently, have different meshing requirements, and were run on different hardware. Therefore, our goal here is to give the reader a general appreciation for the computational hardware requirements typical for this kind of numerical modeling work.

Toward this end, several metrics were identified as useful in highlighting the similarities and differences in the characteristic performance of the various codes. These metrics include: mesh size (spatial step size) in the pristine and defect regions, time step size, simulation run time, number of degrees of freedom, number of processors on which the simulation was run. This

information is tabulated in Table 5, and shows the advantages and disadvantages of each code from the perspective of computational resources they each require for accomplishing the same simulation task. It is noted that for COMSOL, it was found that if the time step is auto-selected by the COMSOL algorithm, the simulation run time is an order of magnitude longer (235 hours) than the value listed in the table for manually selected time stepping.

For the results presented in this paper and in Table 5, the simulation tools were implemented on different computing hardware(based on availability of hardware and associated licenses, etc). The EFIT code which is parallelized to run on a large number of cores was run on 72 Intel Xeon E7-2850 2.0 GHz processors. COMSOL simulations were run on 16 Intel Xeon E5-2687 3.1 GHz cores. ABAQUS and ANSYS were both implemented on 16 Xeon E5-2697 2.7 GHz processors.

Table 5: Various performance metrics for the simulation codes under study: average mesh size in the (x, y) plane over the pristine and delaminated regions ($\langle \Delta x \rangle_\mathrm{p}$ and $\langle \Delta x \rangle_\mathrm{d}$, respectively); mesh size along panel thickness (Δz); time step (Δt); simulation run time (T_run); number of degrees of freedom (# DoF); number of CPU cores (# cores); and memory required (mem).

Metric ⇒	$\langle \Delta x \rangle_\mathrm{p}$	$\langle \Delta x \rangle_\mathrm{d}$	Δz	Δt	T_run	#DoF	#cores	mem
Method ⇓	(μm)	(μm)	(μm)	(ns)	(hours)	(10^6)	–	(GB)
EFIT	28.75	28.75	28.75	2.19	91	2510	72	142
COMSOL	600	500	57.5	50	19.5	7.77	16	266
ABAQUS/I	500	200	57.5	100	40	1.7	16	28
ABAQUS/E	200	100	57.5	2	53	26	16	30
ANSYS	400	200	57.5	100	170	10	16	16

7. Conclusions

The results discussed in this paper are presented as benchmark studies of four different simulation tools for 3D modeling of ultrasonic waves in CFRP laminates. Three different simulation tools for implicit modeling were implemented: COMSOL, ABAQUS/I and ANSYS. Two explicit approaches were implemented: EFIT and ABAQUS/E. Group velocity and wavenumber domain comparisons were performed for cases of guided wave propagation in a pristine and delaminated CFRP laminates. The comparisons showed that all

simulation tools matched well with theory and also agreed fairly well with experiment. It is expected that more accurate material property values for the experimental case would bring the simulation results into closer agreement with experiment. The spatial and time step requirements of the various tools were presented as guidance to researchers utilizing these tools for similar purposes. Additionally, the computational demands of each simulation tool were given, as such details are often a leading factor in determining the feasibility of a simulation scenario.

Overall, the results show that with the proper configuration, each of the four simulation tools is adequate for simulating the physics of guided wave propagation in CFRP laminates. Future work will include benchmarking simulation tools for cases with higher degrees of anisotropy and cases of complex geometry composites (such as curved and hat-stiffened specimens which are common for aerospace applications). It is expected that further differences between the simulation codes may be observed as the simulation size scales to represent larger specimens and/or to represent complex geometry specimens.

[1] I.M. Daniel, O. Ishai, Engineering mechanics of composite materials, Oxford Univeristy Press, New York, pp. 26–42 (2006).

[2] J. E. Hodgkinson, Mechanical Testing of Advanced Fibre Composites, CRC Press, Boca Raton FL, USA, pp. 175–176 (2000).

[3] C.T. Ng, M. Veidt, L.R.F. Rose, and C.H. Wang, Analytical and finite element prediction of Lamb wave scattering at delaminations in quasi-isotropic composite laminates, J Sound Vibr 331 (2012) 4870–4883.

[4] D. Singh, R. Guerjouma, M. Bentahar, Interaction of fundamental Lamb modes with a point impact damaged zone in composite, Proc Soc Fre Acoust (2012) 2423–2428.

[5] C.A.C. Leckey, M.D. Rogge, F.R. Parker, Guided waves in anisotropic and quasi-isotropic aerospace composites: Three dimensional simulation and experiment, Ultrasonics 54 (2014) 385–394.

[6] B. Murat, P. Khalili, P. Fromme Scattering of guided waves at delaminations in composite plates, J Acoust Soc Amer 139.6 (2016) 3044–3052.

[7] F. Schubert, A. Peiffer, B. Kohler, T. Sanderson, The elastodynamic finite integration technique for waves in cylindrical geometries, J Acoust Soc Am 104 (1998) 2604–2614.

[8] C.A.C. Leckey, J.P.. Seebo, Guided wave energy trapping to detect hidden multilayer delamination damage, Rev Progr Quant Nondestr AIP Publishing, 1650 (2015) 1162–1169.

[9] F. Fellinger, K.J. Langenberg, Numerical techniques for elastic wave propagation and scattering, Proc IUTAM Sym (1990) 81–86.

[10] F. Fellinger, R. Marklein, K.J. Langenberg, S. Klaholz, Numerical modeling of elastic wave propagation and scattering with EFIT - elastodynamic finite integration technique, Wave Motion (1995) 47–66.

[11] R. Marklein, R. Barmann, K.J. Langenberg The ultrasonic modeling code EFIT as applied to inhomogeneous dissipative isotropic and aniostropic media, Rev Prog Quant Nondestr 14 (1995) 251–258.

[12] F. Schubert, B. Koehler, Numerical time-domain simulation of diffusive ultrasound in concrete, Ultrasonics 42 (2004) 781–786.

[13] R. Marklein, The finite integration technique as a general tool to compute acoustic, electromagnetic, elastodynamic, and coupled wave fields, Rev Radio Sci: 1999-2002 URSI, edited by W. Stone, IEEE Press and John Wiley and Sons, New York, pp. 201–244 (2002).

[14] S. Halkjaer, M.P. Sorensen, W.D. Kristensen, The propagation of ultrasound in an austenitic weld, Ultrasonics 38 (2000) 256–261.

[15] K. Nakahata, S. Hirose, F. Schubert, B. Kohler, Image based EFIT simulation for nondestructive ultrasonic testing of austenitic stell, J Solid Mech Mater Eng 3 (2009) 1256–1263.

[16] J.P. Bingham, M.K. Hinders, Lamb wave characterization of corrosion-thinning in aircraft stringers: Experiment and three-dimensional simulation, J Acoust Soc Am 126 (2009) 103–113.

[17] F. Schubert, Numerical time-domain modeling of linear and nonlinear ultrasonic wave propagation using finite integration techniques - theory and applications, Ultrasonics 42 (2004) 221–229.

[18] K.E. Rudd, K.R. Leonard, J.P. Bingham, M.K. Hinders, Simulation of guided waves in complex piping geometries using the elastodynamic finite integration technique, J Acoust Soc Am 121 (2007) 1449–1458

[19] J.P. Bingham, M.K. Hinders, 3D elastodynamic finite integration technique simulation of guided waves in extended built-up structures containing flaws, J Comput Acoust 18 (2010) 165–192.

[20] C.A.C. Leckey, M.D. Rogge, C.A. Miller, M.K. Hinders, Multiple-mode lamb wave scattering simulations using 3D elastodynamic finite integration technique, Ultrasonics 52 (2012) 193–207.

[21] L. Yu, C.A.C. Leckey, Lamb wave based quantitative crack detection using a focusing array algorithm, J Intelligent Mater Syst Struct, 24.9 (2013) 1138-1152.

[22] Hexcel, `http://www.hexcel.com/Resources/DataSheets/Prepreg-Data-Sheets/8552_eu.pdf`, date last viewed 5/17/2012.

[23] P.P. Camanho, P. Maimi, C.G. Davila, Prediction of size effects in notched laminates using continuum damage mechanics, Compos Sci Technol 67 (2007) 2715–2727.

[24] A.S. Kaddour, M.J. Hinton, S. Li, P. Smith, Instructions to the contributors of the third world-wide failure exercise (WWFE-III): part A, (2008).

[25] B.N. Pavlakovic, M.J.S. Lowe Disperse: a general purpose program for creating dispersion curves, Rev Prog Quant Nondestr 16A (1997) 155–192.

[26] M. Rogge, C. Leckey, Characterization of impact damage in composite laminates using guided wavefield imaging and local wavenumber domain analysis, Ultrasonics 53.7 (2013) 1217-1226.

[27] P. Juarez, C. Leckey, Multi-frequency local wavenumber analysis and ply correlation of delamination damage, Ultrasonics 62 (2015) 56-65.

[28] Z. Tian, L. Yu, C.A.C. Leckey, Delamination detection and quantification on laminated composite structures with Lamb waves and wavenumber analysis, J Intelligent Mater Syst Struct, 26.13 (2015) 1723-1738.

[29] ABAQUS Analysis User's Manual, ABAQUS® Standard, Version 6.14, Dassault Systemes Simulia Corp., Providence, RI 2017.

[30] ANSYS Mechanical User's Guide, ANSYS®, Release 15.0, ANSYS Inc., Canonsburg, PA, 2013.

[31] COMSOL Multiphysics®, Version 5.2a, COMSOL AB, Stockholm, Sweden, 2017.